**Key Points:**
- When flash-frozen, fluids representative of Enceladus' ocean form ice-templated brines that can crystallize or undergo vitrification
- The 10 µm-scale distribution of crystalline salt phases records a signature diagnostic of cooling rate
- Mineralogy of cryogenic Na-carbonates is dependent on pH and cooling rate, with bicarbonates kinetically inhibited during flash-freezing

**Supporting Information:**
- Supporting Information S1
- Movie S1

**Correspondence to:**
M. G. Fox-Powell,
mark.fox-powell@open.ac.uk

# Partitioning of Crystalline and Amorphous Phases During Freezing of Simulated Enceladus Ocean Fluids

**Mark G. Fox-Powell[1,2]** , and **Claire R. Cousins[1]**

[1]School of Earth and Environmental Sciences, University of St Andrews, St Andrews, UK, [2]Now at AstrobiologyOU, The Open University, Milton Keynes, UK

**Abstract**  Saturn's ice-covered moon Enceladus may contain the requisite conditions for life. Its potentially habitable subsurface ocean is vented into space as large cryovolcanic plumes that can be sampled by spacecraft, acting as a window to the ocean below. However, little is known about how Enceladus' ocean fluids evolve as they freeze. Using cryo-imaging techniques, we investigated solid phases produced by freezing simulated Enceladean ocean fluids at endmember cooling rates. Our results show that under flash-freezing conditions ($>10$ K s$^{-1}$), Enceladus-relevant fluids undergo segregation, whereby the precipitation of ice templates the formation of brine vein networks. The high solute concentrations and confined nature of these brine veins means that salt crystallization is kinetically inhibited and glass formation (vitrification) can occur at lower cooling rates than typically required for vitrification of a bulk solution. Crystalline salts also form if flash-frozen fluids are re-warmed. The 10 µm-scale distribution of salt phases produced by this mechanism differs markedly from that of gradually cooled ($\sim$1 K min$^{-1}$) fluids, showing that they inherit a textural signature of their formation conditions. The mineralogy of cryogenic carbonates can be used as a probe for cooling rate and parent fluid pH. Our findings reveal possible endmember routes for solid phase production from Enceladus' ocean fluids and mechanisms for generating compositional heterogeneity within ice particles on a sub-10 µm scale. This has implications for understanding how Enceladus' ocean constituents are incorporated into icy particles and delivered to space.

**Plain Language Summary**  Enceladus, a moon of Saturn, contains a global subsurface ocean that interacts with a rocky seafloor, potentially generating the necessary conditions for life. Large plumes, erupting from cracks in Enceladus' south polar region, were sampled by the Cassini spacecraft and found to originate from the ocean, providing a route to studying its composition and habitability. We used up-to-date constraints on Enceladus' ocean chemistry to experimentally investigate the formation of icy particles within these plumes, focusing on the fate of dissolved ocean components during freezing at contrasting freezing rates. Using cryo-imaging techniques, we show that fluids segregate into ice and nonice even at flash-freezing conditions (more than 10°C per second). By studying the salt minerals that formed in our experiments, we show that their composition and microscale distribution can record information about fluid alkalinity and freezing rate. Our results will help interpret data from the Cassini mission and provide a strong rationale for future nondestructive measurements of the Enceladus plumes as well as plumes at other ocean-bearing worlds, such as Jupiter's moon Europa.

## 1. Introduction

The Saturnian moon Enceladus exhibits large cryovolcanic plumes sourced from a subsurface liquid water reservoir (Postberg et al., 2011) thought to be a global subsurface ocean (Choblet et al., 2017; P. C. Thomas et al., 2016). Observations made by the Cassini spacecraft revealed that these plumes contain evidence of endogenic organic chemistry and hydrothermal activity at the core-ocean boundary (Hsu et al., 2015; Postberg et al., 2018; Waite et al., 2017), encouraging comparisons with favored scenarios for the emergence of life on Earth (Deamer & Damer, 2017; McKay et al., 2014), and demonstrating that microbial metabolisms such as methanogenesis are feasible at Enceladus today (Taubner et al., 2018; Waite et al., 2017). These factors, alongside the relative accessibility of the plumes to spacecraft, mean Enceladus is viewed as high-priority target for astrobiology (Hendrix et al., 2019).

Cryovolcanic plumes on Enceladus emanate from aligned vent structures ("tiger stripes") at the moon's south polar region (Porco et al., 2006). Salt-rich "Type III" ice particles observed in the plumes by Cassini's Cosmic Dust Analyzer (CDA) (Postberg et al., 2009) are interpreted as rapidly frozen spray from a body of liquid water that likely interacted with rock (Porco et al., 2006). This implies that, unlike other populations of particles that may condense from vapor (Postberg et al., 2011, 2018), Type III particles most closely represent ocean composition. Studying them can provide a means of probing the habitability and potential biology of an extraterrestrial ocean, an approach pioneered by the Cassini mission (Postberg et al., 2009, 2018; Waite et al., 2009, 2017) and proposed for future missions (Reh et al., 2016).

A crucial step in understanding these Type III particles is to determine the composition and sequence of solid phases that form upon freezing of Enceladus' ocean fluids. Bulk composition of Type III particles and the low abundance of $CO_2$ in the plumes inferred by Cassini observations implies that Enceladus hosts a sodium, chloride and carbonate-dominated ocean with an alkaline pH around 9 (Glein et al., 2015; Glein & Waite, 2020; Waite et al., 2017). Equilibrium models investigating gradual freezing of an early ocean on Enceladus predicted, prior to CDA analyses of the plumes, that sodium carbonate and sodium chloride salts should be major products (Zolotov, 2007). These phases are also predicted by equilibrium models to form during cooling of Ceres cryomagmas and alteration fluids on CI chondrites, which likely share similar chemistry with Enceladus (Quick et al., 2019; Zolotov, 2012, 2017). However, based on models of the thermal and pressure conditions inside the vents (Nakajima & Ingersoll, 2016), droplets of Enceladus' ocean fluid may cool extremely rapidly, freezing in <1 ms (Glein & Waite, 2020). As cooling rate increases, kinetics of crystallization become increasingly important for defining the solid products of freezing, and predictions based on chemical equilibria can become unreliable.

### 1.1. Cooling Rate and Kinetic Effects on Freezing

In a closed system, if all components remain at chemical equilibrium during cooling, solutes are excluded from crystallizing ice and concentrated; eventually precipitating as solids in a sequence that can be predicted from chemical thermodynamics. Precipitation events, also termed "chemical divides," can alter ion ratios in the remaining solution, thus determining subsequent fluid evolution (Eugster & Hardie, 1978). Predictions of this behavior under equilibrium conditions have been widely employed to investigate the origins of salt mineral assemblages on the surfaces of Europa (Johnson et al., 2019), Ceres (Quick et al., 2019; Zolotov, 2017), and Mars (King et al., 2004; Toner et al., 2015; Tosca & McLennan, 2006), and the early differentiation and freezing of Enceladus' ocean (Zolotov, 2007).

Achieving complete equilibrium in nature or in the laboratory was originally thought to require long equilibration times (i.e., several weeks) (G. Marion et al., 1999), but recent experimental studies of freezing of terrestrial seawater have shown that cooling rates typical of those experienced by natural sea ice (~1 K h$^{-1}$) can produce mineral assemblages close to the chemical equilibrium composition (Butler & Kennedy, 2015).

As cooling rates increase, true equilibrium crystallization can be inhibited and a metastable assemblage of solid phases produced. One pathway for this to occur is *via* fractional crystallization, whereby precipitated phases are prevented from interacting with residual brines; a plausible outcome where mineral precipitation and dissolution kinetics are slow and outpaced by cooling rate (Zolotov & Shock, 2001), or the spatial heterogeneity of the ice matrix limits brine/mineral interaction. Depending on fluid composition, fractional crystallization can profoundly affect freezing behavior. For example, experimental observations of terrestrial seawater freezing have demonstrated that whether or not mirabilite ($Na_2SO_4 \cdot 10H_2O$), an early precipitate, is permitted to dissolve later in the sequence controls whether gypsum ($CaSO_4 \cdot 2H_2O$) or antarcticite ($CaCl_2 \cdot 6H_2O$) will subsequently form, driving a difference of 18 K in eutectic temperature (Marion et al., 1999).

If cooling rate is sufficiently high, thermal energy may be removed from a system more rapidly than crystal growth can occur, resulting in the inhibition of crystallization and the formation of glass. Bulk vitrification (glass formation) in dilute solutions has been intensively studied for cryopreservation industry applications (Wowk, 2010), and requires extremely rapid cooling rates (>$10^6$ K s$^{-1}$ for pure water; Hallbrucker & Mayer, 1988). High concentrations of solutes and confinement of fluid within microporous spaces, both features of residual brines concentrated by ice formation, can act synergistically to impede crystallization (Gallo et al., 2016). This may allow partial vitrification to occur at slower cooling rates than those required to vitrify

**Table 1**
*Theoretical and Experimental Ionic Composition of Simulated Enceladus Fluids*

| | Theoretical concentration | Experimental concentration | |
| --- | --- | --- | --- |
| | | pH 11 | pH 9 |
| $Cl^-$ | 200.000 | 201.151 | 221.151 |
| $HCO_3^-/CO_3^{2-}$ | 70.000 | 70.000 | 70.000 |
| $NH_3/NH_4^+$ | 1.000 | 1.000 | 1.000 |
| $Na^+$ | 340.000 | 344.702 | 302.480 |
| $K^+$ | 2.267 | 2.267 | 2.267 |
| $SiO_2$ | 3.329 | 3.329 | 3.329 |

*Note.* All in mmol per kg $H_2O$.

bulk solutions, leading to products comprising both crystalline and amorphous phases. For example, vitrification of freeze-concentrated solutions between ice crystals has been demonstrated experimentally in dilute $Na^+/Cl^-$ brines at cooling rates of $10^1$–$10^2$ K s$^{-1}$ (Imrichová et al., 2019).

The kinetically limited behavior typical of rapid cooling is not well parameterized in predictive models, hence must be investigated empirically. Recent experimental studies have revealed pronounced cooling rate effects; for example, the formation of sodium salts was observed in simulated Ceres-relevant fluids during freezing at 30 K min$^{-1}$ (Vu et al., 2017), but kinetically inhibited during flash-freezing in liquid nitrogen (Thomas et al., 2019); and Mg-rich fluid compositions that may exist at Europa produced crystalline Mg chloride salts when cooled at 1 K min$^{-1}$, but glass when flash-frozen (Vu et al., 2020).

Here, we experimentally investigated the production and partitioning of solid phases during freezing of fluids designed to simulate Enceladus' ocean. We investigated contrasting cooling rates: (i) flash freezing (>10 K s$^{-1}$), using the liquid nitrogen approach previously established (Thomas et al, 2017, 2019; Vu et al., 2020), and (ii) slow freezing (~0.01 K s$^{-1}$), comparing our findings with chemical thermodynamic predictions of equilibrium and fractional crystallization. We also examined the further effects of re-warming of flash-frozen fluids from liquid nitrogen temperatures, and of confinement in microporous spaces, where fluids were cooled gradually (0.01 K s$^{-1}$), but were restricted to a 60 μm-thick film. Our findings provide new endmember constraints on the range of solid products produced by cryovolcanism at Enceladus.

## 2. Materials and Methods

### 2.1. Simulated Enceladus Ocean Fluids

Fluid compositions for simulating Enceladus' ocean were designed based on up-to-date constraints provided by both *Cassini* data and computational efforts. Table 1 gives the targeted (theoretical) concentrations of each ion and the actual (experimental) concentration used for experiments. Theoretical concentrations were selected individually for each ion, based on the rationale described below, and therefore do not necessarily form a charge-balanced solution. The difference between theoretical and experimental concentrations arises from the need to use salt compounds in the laboratory, which do not match the stoichiometry of the targeted concentrations. The rationale for each ion's concentration, reported here in millimoles per kilogram of water, is as follows:

*Chloride:* 200 mmol represents the overlap between complementary analytical approaches (ice particle analysis by CDA; Postberg et al., 2009) and mass balance calculations (assuming total extraction of Cl− from a CI chondritic core; Glein et al., 2015). Full ranges were: 50–200 mmol (analytical); 200–1,200 mmol (modeled).

*(Bi)carbonate:* A concentration of 70 mmol dissolved inorganic carbon (DIC) was selected to match that used by Glein et al. (2015) and Waite et al. (2017) in alkalinity calculations. The value is the upper-mid range originally constrained by CDA measurements of plume particles (full analytical range: 40–100 mmol) (Postberg et al., 2009). At pH 11, all is in the form $CO_3^{2-}$, whereas at pH 9, $HCO_3^-$ dominates at an $HCO_3^-/CO_3^{2-}$ ratio of approximately 5 (at 10°C, see Figure S2).

*Sodium:* A concentration of 340 mmol Na was targeted based on CDA measurements of ice particles, and includes the contribution from NaCl and Na-carbonates used to replicate CDA data in analog experiments (Postberg et al., 2009). Full range 90–400 mmol.

*Potassium:* The targeted K concentration is defined by the mid-range Na/K ratio identified from plume particle analysis (Postberg et al., 2009) (150; full range 100–200).

*Silica:* The observed abundance of silica nanoparticles associated with Enceladus requires that the ocean is supersaturated with respect to amorphous silica (Hsu et al., 2015). As these nanoparticles were encountered freely in space, and not in association with salt-rich ice particles, we did not include silica colloids, and instead focused our experiments on the behavior of species that are in solution at

**Table 2**
*Simulated Enceladean Ocean Fluid Recipes, in g kg $H_2O^{-1}$*

|  | pH 11 | pH 9 |
|---|---|---|
| NaCl | 11.550 | 12.719 |
| $Na_2CO_3$ | 7.419 | 0.824 |
| $NaHCO_3$ | – | 5.227 |
| $NH_4Cl$ | 0.053 | 0.053 |
| KCl | 0.248 | 0.248 |
| $Na_2SiO_3$ | 0.406 | 0.406 |

the onset of freezing. We assume that aqueous silica in the ocean fluids is close to the saturation point of amorphous silica at 273 K and pH 9 (as solubility sharply increases above 10.5), and therefore included 200 ppm (3.3289 mmol).

*Ammonia/ammonium:* As a gas in the plumes, $NH_3$ is present at between 0.4% and 1.3% (Waite et al., 2017). If plume gases were condensed directly to form a liquid, this would result in a concentration of approximately 230–760 mmol $NH_3/NH_4^+$. However, fractional distillation of gases in the vents is expected, preferentially condensing water vapor and enriching $NH_3$ and other compounds. Using Equation 1 in Glein et al. (2015) to account for the maximum possible distillation provided an estimate of oceanic $NH_3/NH_4^+$ of 0.0007 mmol. The range of possible concentrations therefore spans seven orders of magnitude. We took 1 mmol as an approximate mid-range estimate, a value that should be updated in response to more accurate constraints on $NH_3/NH_4^+$.

*pH*: Due to the likelihood that oceanic $CO_2$ is present at relatively low concentrations, a highly alkaline pH is favored, recently estimated as around 9 (Glein & Waite, 2020). We include both pH 9 and pH 11 fluids for two main reasons. First, pH 11 remains a realistic maximum based on plume gas measurements (Waite et al., 2017). Second, this range provides an experimental advantage as it spans the major alkaline pH-induced ionic changes in this system, including $HCO_3^-/CO_3^-$ and $NH_3/NH_4^+$ speciation and the solubility inflection point of aqueous silica, allowing us to observe the cryogenic products of a low and high pH regime even if the true value falls outside our range.

### 2.2. Synthesis of Fluids

Ionic compositions described above were converted to salt compounds (see Table 2). Ultra-pure water was purged of $O_2$ by sparging with $N_2$ gas for 40 min. Fluids were synthesized by dissolving all salts except $Na_2SiO_3$ in $N_2$-sparged water and making up to 80% final volume. A separate solution of $Na_2SiO_3$ was made up to 20% final volume in $N_2$-sparged ultra-pure water and adjusted to the correct pH with HCl. These two solutions were then combined, sparged with $N_2$ for 40 min and stored under $N_2$ atmosphere at room temperature until use. Following final sparging, pH was confirmed to fall within 0.05 pH units of the target level.

### 2.3. Freezing Experiments

Flash-freezing experiments were performed by dripping ~4 µl aliquots of room-temperature (293 K) simulated Enceladean ocean fluids into liquid $N_2$ ($LN_2$). These produced droplets with a radius of approximately 1 mm. Slow-freezing experiments were performed by placing 20 ml of room temperature fluid on a Petri plate into a 233 K chiller. Temperature of the fluid was monitored with a Traceable Digital Thermometer (Fisherbrand) (Figure S1). Visual observations confirmed complete solidification after approximately 90 min. A further experiment was carried out whereby fluids were gradually cooled (0.01 K s$^{-1}$) as a thin film (~60 µm thick) between two glass slides (see Section 2.5). To prepare samples for bulk analyses, frozen fluids were kept at 233 K and ~3 millibar for approximately 80 h in the condenser section of a Heto Power-Dry LL3000 Freeze Drier to sublimate ice. Dry cryogenic salts were then stored under a dry $N_2$ atmosphere at room temperature prior to analysis.

### 2.4. Scanning Electron Microscopy

Cryo-SEM was performed at the University of Edinburgh using a Zeiss Crossbeam 550 integrated with a Quorum Technologies PP3010 Cryo-stage, airlock and cryo-prep bench. Frozen droplets were mounted on pre-chilled SEM stubs using Cryo-glue (Quorum Technologies), transferred into the airlock using an insulated sample transfer container at 123 K and fractured open using a scalpel blade in the chilled (123 K) prep chamber. Sublimation was carried out at 183 K and $10^{-7}$ millibar for increments of 10 min. After 30 min

total sublimation, ices were sputter-coated with palladium before being imaged at 8 KeV using secondary and backscatter electron detectors.

Cryogenic precipitates removed from ice by complete sublimation were analyzed at room temperature at the University of Glasgow using the secondary electron detector of a Carl Zeiss SIGMA HD VP Field Emission SEM. Samples were gold- and palladium-coated and imaging carried out at an accelerating voltage of between 5 and 20 KeV. Energy-dispersive spectroscopy (EDS) point analyses were carried out at an accelerating voltage of 20 KeV.

### 2.5. Optical Microscopy

Optical microscopy was performed using a Leica DM4000B digital microscope integrated with a Linkam THMS600 cooling stage at the University of Edinburgh. Images were acquired using a Leica DFC 450 C microscope-mounted camera. Cooling was performed in a 250 µl crucible for examining eutectic crystallization at 0.01 K s$^{-1}$, or as a film between glass slides for observation of freezing as a thin film at 0.01 K s$^{-1}$. The film had a maximum depth of approximately 60 µm. After cooling to 172 K, thin film samples were warmed back to room temperature at a rate of 10 K min$^{-1}$ (0.17 K s$^{-1}$).

### 2.6. X-ray Diffraction

Powder X-ray diffraction patterns were recorded from ice-free (sublimated) cryogenic precipitates in the School of Earth and Environmental Sciences, University of St Andrews, UK. Measurements were made in reflection mode at room temperature with Co K$\alpha$1,2 radiation (1.790307 Å) operating at 30 kV and 30 mA, from 3° to 70° (2θ) at a scan rate of 0.01° (2θ)/second using a Philips PW1830 generator, PW1710 diffractometer control and PW1050/80 goniometer. Phase identification was carried out by matching to the International Center for Diffraction data (ICDD) Powder Diffraction File database.

### 2.7. Thermodynamic Simulations of Freezing

The precipitation of salts from simulated Enceladean ocean fluids during freezing was predicted using FREZCHEM (ver. 15.1) (Marion et al., 2010), which implements Pitzer equations to calculate activity coefficients at low temperatures. Ionic compositions from the "experimental" columns in Table 1 were used as inputs, with initial pCO$_2$ of either $9 \times 10^{-4}$ bar (pH 9) or $1 \times 10^{-6}$ bar (pH 11). The former was the mid-range favored oceanic CO$_2$ concentration from Cassini INMS plume measurements (Glein & Waite, 2020), while the latter was required to achieve pH 11 in this chemical system. The pCO$_2$ was included as an output parameter; that is, it was allowed to vary during model runs.

Predictions were generated for both equilibrium and fractional crystallization scenarios from a starting solution containing 1,000 g H$_2$O until < 0.1 g liquid H$_2$O remained. Temperature was decreased in 0.1 K increments. Equilibrium crystallization scenarios calculate equilibrium between all solid and solution components at each temperature step, while fractional crystallization scenarios do not allow solid phases to react with residual solution components once precipitated. Simulations were repeated at 1 bar and 15 bar with minor (maximum 1 K) variation in predicted mineral formation temperatures, and no change in mineral formation sequence. Only 1 bar simulations are reported here. Excess aqueous silica was generated by the model for charge balance, thus the molalities of individual Si species reported here were normalized to the starting molality of Si. Due to the lack of thermodynamic parameterization of silica speciation and solubility above pH 10.5, silica was removed from FREZCHEM pH 11 runs. At pH 10.5, FREZCHEM predicted that amorphous silica should begin to precipitate at 276 K; this is indicated in Figure S2.

### 2.8. Estimates of Experimental Cooling Rates

The cooling rate experienced by fluids during flash freezing in LN$_2$ was stimated *via* a two-step process. First, the maximum theoretical heat loss from a room-temperature (293 K) droplet injected into a 77 K ambient environment was calculated for droplets of radius, *r* = 1 mm. In small droplets that cool very rapidly,

conductive heat loss is the dominant process (Song et al., 2010), so this can be approximated using the heat flow equation:

$$Q = \frac{kA\left(T_{\text{amb}} - T_{\text{fluid}}\right)}{r} \tag{1}$$

where $Q$ is the rate of heat transfer, in J s$^{-1}$, $k$ is the thermal conductivity of the material, $A$ is the surface area over which heat is transferred, and $T_{\text{amb}}$ and $T_{\text{fluid}}$ represent the temperature of the environment into which the fluid is introduced (77 K) and the initial temperature of the fluid (293 K), respectively. We assumed that thermal conductivity was equal to that of seawater (0.6 W/mK at 298 K), which has been observed to decrease by approximately 0.3% per degree Kelvin (Caldwell, 1974), thus our estimates made allowances for this by averaging $k$ over the temperature change. The adjusted $k$ value was 0.439 W/m K (for $T_{\text{amb}} = 77$ K). Conductive cooling rate in change in degrees K ($\Delta$K) per second was then calculated via the following:

$$\Delta\text{Ks}^{-1} = \frac{Qm^{-1}}{c} \tag{2}$$

where $m$ is the mass of the fluid and $c$ is the specific heat of the fluid (assumed here to be equal to that of terrestrial seawater). Specific heat was assumed constant, as the effect of temperature is negligible near 273 K (Sharqawy et al., 2010). Density of the simulated Enceladus fluid was measured at 1.015 g cm$^{-3}$. Using Equations 1 and 2, we calculated a maximum theoretical conductive cooling rate of 63.3 K s$^{-1}$.

Next, we considered for the tendency for rapidly boiling N$_2$ to form an envelope of insulating gas around a droplet of warmer fluid (the reverse Leidenfrost effect), resulting in effectively slower cooling than the maximum theoretical rate calculated above. Relatively warm droplets introduced into a cryo-liquid such as LN$_2$ either remain at the surface or become submerged but encased in gas for several seconds (Adda-Bedia et al., 2016) until a threshold temperature (the Leidenfrost temperature) is reached, after which the reverse Leidenfrost effect ceases and insulation is lost. Adda-Bedia et al. (2016) show that droplets of a similar radius (~1 mm) and density (1.02 g cm$^{-3}$) to the simulated Enceladean ocean fluids took approximately 12 s to reach the Leidenfrost temperature (126 K for nitrogen) from 293 K, corresponding to a cooling rate of 13.9 K s$^{-1}$. In our experiments, droplets never took longer than 12 s to sink. We therefore assume that the cooling rate experienced was between 13.9 K s$^{-1}$ (maximum reverse Leidenfrost effect) and 63.3 K s$^{-1}$ (no reverse Leidenfrost effect; conductive cooling only).

## 3. Results

### 3.1. Physical Partitioning of Ice and Non-Ice Components

Imaging at 123 K of the immediately partitioned ice and nonice components within flash-frozen droplets (cooling rate between 13.9 and 63.3 K s$^{-1}$) reveals a solidified ice-templated brine vein network at ice grain boundaries (Figures 1a–1d and S3). Subsequent ice sublimation did not alter the structure or appearance of this network (Figures 1a–1c). Within a ~100 μm region at the surface of the droplet the ice grain voids in the vein network are considerably smaller than the bulk droplet (Figure 1e), across which ice grain void sizes are relatively constant (Figure 1d). We measured brine vein dimensions across a ~54,000 μm$^2$ region of the fractured droplet interior and estimate that brine veins comprise ~5% of the total droplet cross-sectional area.

A similar ice-templated vein network is also observed under the slow freezing regime (average cooling rate 0.01 K min$^{-1}$; Figure S1), producing larger ice grain voids (Figure 1g). After complete sublimation of ice this vein structure remains intact (Figures 1f and 1g). Ice-free broken up cryogenic particles bear morphological features similar to those previously identified in terrestrial ice-templated cryogenic opal-A (COA), such as triple-junctions, branched threads and sheets (Channing & Butler, 2007; Fox-Powell et al., 2018; Figure S4).

### 3.2. Formation of Cryogenic Precipitates Within Brine Veins

Cryo-SEM imaging reveals smooth, glass-like noncrystalline material at ice grain boundaries within flash-frozen samples (Figure 2a). This material contains bubbles with roughly circular cross-sections
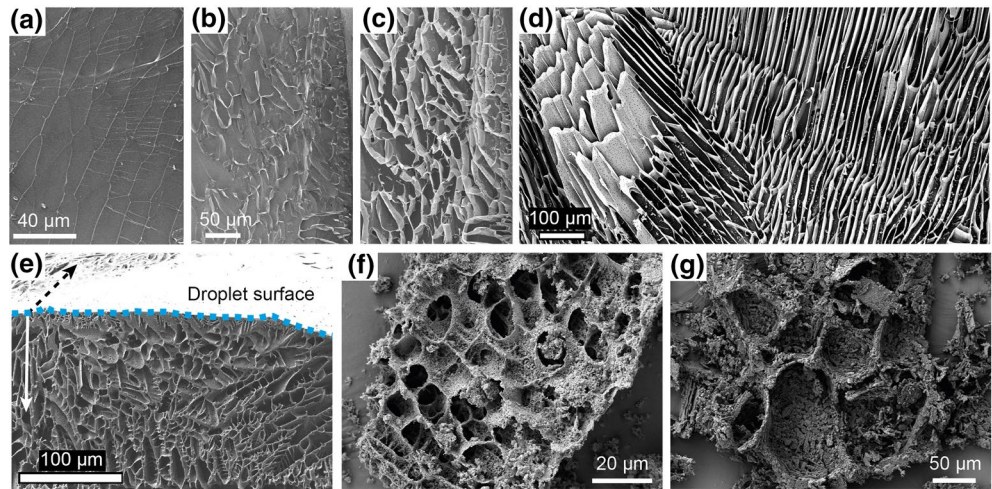
**Figure 1.** Cryo-SEM (a–e, imaged at 123 K) and SEM (f and g, imaged at room temperature) images of experimental products. (a) Interior cross-section of a flash-frozen droplet of simulated Enceladean ocean fluid, showing ice (dark material) and solidified brine veins (threads of lighter material). (b and c) Interior of a flash-frozen droplet after 10 (b) and 20 (c) min of sublimation. (d) Interior of flash-frozen droplet after 30 min of sublimation showing solidified vein network. (e) Outermost region of flash-frozen droplet, showing vein network nearest to the droplet surface, after 30 min of sublimation. Arrows illustrate $z$-plane orientation of droplet surface relative to interior cross-section. (f) Flash-frozen sample following complete sublimation of ice. (g) Slow-frozen sample following complete sublimation of ice.

distributed evenly throughout (Figures 2a and S4), similar to bubbles formed in the brine veins of gradually cooled (∼0.01 K s$^{-1}$) 60 μm-thick films, observed via optical microscopy (Figure 2b). These restricted thin-film brine veins do not crystallize upon cooling to a minimum of 172.98 K. Following subsequent re-warming, apparently crystalline materials are observed to form in the flash-frozen samples (Figures 2e and 2g), and optical microscopy shows that crystallization of thin film brine veins occurs ∼27 K below the temperature at which ice begins to enter the liquid phase (∼250 K) (Figure 2c). The resulting materials are confirmed as crystalline by X-ray diffraction (see Section 3.4). Crystal assemblages formed through re-warming of flash-frozen fluids are distributed randomly at the 10 μm scale throughout the ice-templated veins (Figures 2e and 2g).
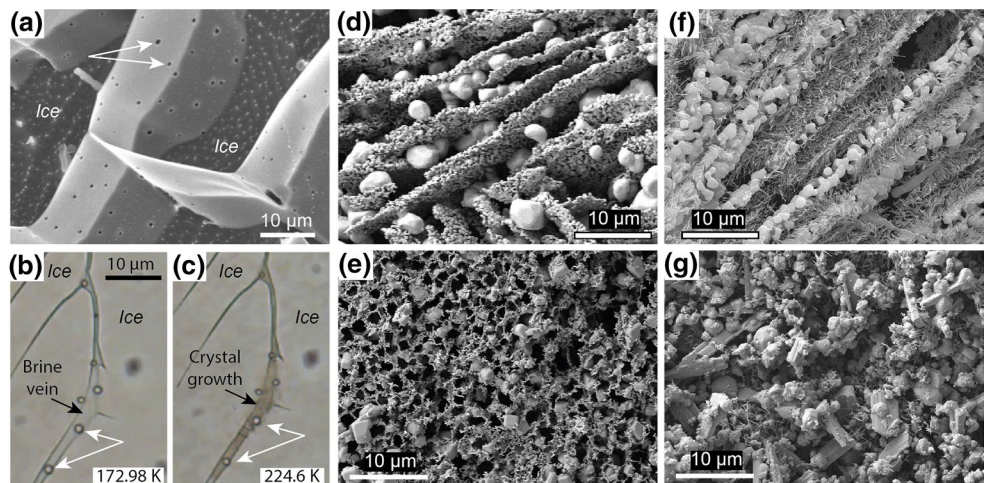


**Figure 2.** a) CryoSEM (123 K) detail of solidified brine vein (smooth light material) after flash-freezing and partial ice sublimation, showing incorporation of bubbles (white arrows). Dark material is water ice. (b and c) Optical microscope images of brine veins cooled as a thin film and rewarmed at a rate of ∼0.17 K s$^{-1}$ White arrows indicate exsolved bubbles. (d–g) Room-temperature SEM images showing the structure of cryogenic salts following complete ice removal. (d) Slow frozen pH 11; (e) flash-frozen and rewarmed pH 11; (f) Slow-frozen pH 9; (g) Flash-frozen and rewarmed pH 9.
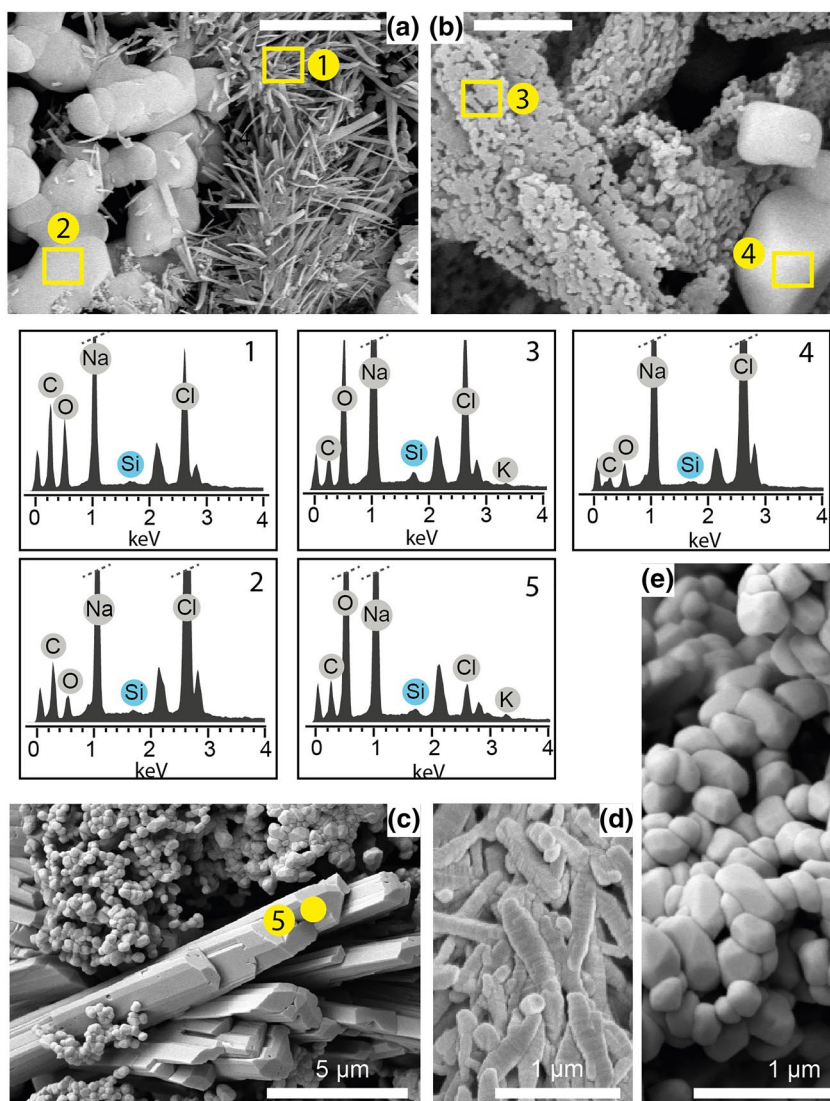
**Figure 3.** Composition of cryogenic salts formed via slow freezing, measured by energy dispersive X-ray spectroscopy (EDS), from pH 9 (a) and pH 11 (b and c) fluids, highlighting the partitioning of Na-chloride and Na-carbonate minerals. Point EDS spectra show counts per second per keV, collected from the indicated regions. Diagonal dashed lines indicate truncated peaks. Scale bars are equal to 5 μm. (d) Detail of foliated filiform cryogenic crystals formed from pH 9 fluids; (e) Detail of botryoidal cryogenic crystals formed from pH 11 fluids.

When fluids are cooled gradually at ~0.01 K s$^{-1}$ in unrestricted larger volumes (≥250 μl; slow freezing regime), brine vein crystallization occurs at around 245 K, confirmed by optical microscopy (Movie S1). At the 10 μm scale, the crystallized brine veins produced by slow freezing exhibit lamellar or globular clusters of distinct crystal types that form repetitive structures (Figures 2d and 2f). Crystals are euhydral of broadly three habits, revealed by the sublimation of ice: 2–8 μm cubic crystals (Figures 3a and 3b), 10–15 μm columnar crystals (Figure 3c) and a large population of smaller crystals (0.1–0.5 μm), which at pH 11 are rounded and botryoidal (Figures 3b, 3c, and 3e) but at pH 9 are filiform and clearly foliated at high magnification (Figures 3a and 3d). Compositional analyses via EDS confirms the small crystals and the larger columnar crystals are Na-carbonates, while the cubic crystals are Na-chlorides (Figures 3a–3c). Hydration state of the salts is not determined by this approach. Similar crystal types are observed in flash-frozen samples following re-warming (Figures 2e and 2g). Although colloidal opal-A is not observed in our experimental precipitates under SEM for either freezing rate, Si is seen to associate preferentially with Na-carbonates, particularly at pH 11 (Figures 3a–3c).
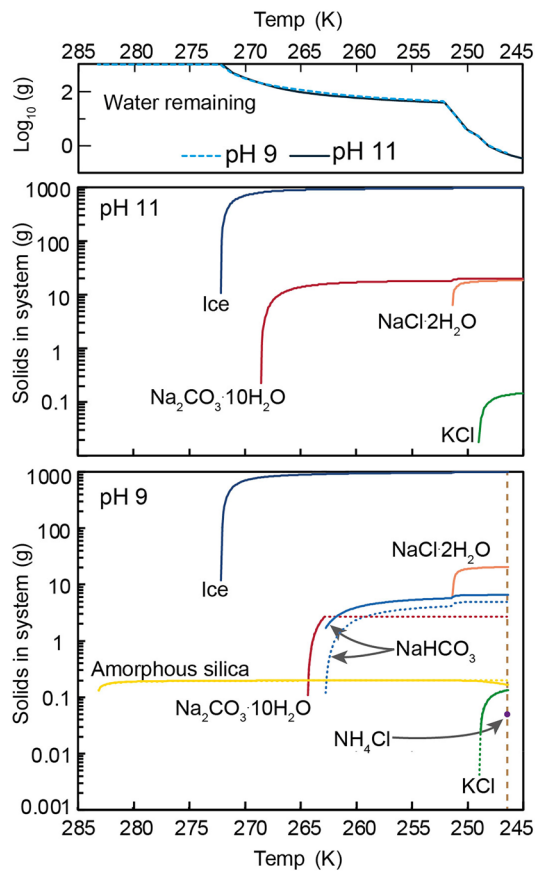
**Figure 4.** Results of FREZCHEM simulations, showing predicted mineral abundances (per kg $H_2O$) as a function of temperature. Where they differ from equilibrium crystallization predictions, fractional crystallization predictions are indicated by dotted lines. The predicted eutectic point is indicated for pH 9 parent fluids by a dashed line at 246.45 K. The predicted eutectic for pH 11 parent fluids is 227.05 K (see text).

### 3.3. FREZCHEM Simulations of Cryogenic Salt Formation

Both equilibrium and fractional crystallization FREZCHEM simulations (Figure 4, Table 3) predict the eutectic point of pH 11 fluids to be considerably lower than that for pH 9 fluids (227.05 K vs. 246.45 K). All ammonic nitrogen is present as $NH_3$ in the former, which continues to accumulate in the late stage brine (Figure S2), whereas at pH 9, ammonium chloride ($NH_4Cl$) precipitates at 246.45 K. The sequence of mineral formation is similar at both parent fluid pH levels. Calculations show that ice formation is depressed by approximately 2 K relative to pure $H_2O$, preceding the formation of Na-carbonates and eventually Na and K (and $NH_4$) chlorides as the eutectic point is approached. From pH 11 fluids, all DIC precipitates as $Na_2CO_3·10H_2O$, whereas at pH 9 this phase forms for only a narrow temperature window before nahcolite ($NaHCO_3$) precipitation becomes dominant.

In the equilibrium crystallization scenario at pH 9, $Na_2CO_3·10H_2O$ redissolves entirely upon nahcolite formation and does not appear in the final eutectic mineral assemblage (Table 3). This results in a higher abundance of nahcolite in the equilibrium crystallization scenario than in the fractional crystallization scenario, in which $Na_2CO_3·10H_2O$ remains. Fractional and equilibrium crystallization predictions are almost identical at pH 11, with differences in mineral abundance at the <<0.1 wt% level (Table 3).

Hydrohalite ($NaCl·2H_2O$) is the dominant salt by weight at pH 9 after complete freezing, but at pH 11 hydrohalite and $Na_2CO_3·10H_2O$ have similar predicted abundances. Halite (NaCl) is not predicted to form at these temperatures. At pH 9, aqueous silica should begin precipitating as amorphous silica before ice forms.

### 3.4. Mineralogy of Experimental Cryogenic Salts

XRD patterns (Figure 5) show that both pH 11 and 9 fluids form halite and sylvite (KCl). At pH 11, thermonatrite ($Na_2CO_3·H_2O$) is the major carbonate phase under both freezing regimes, with possible trace quantities of trona ($Na_2CO_3·NaHCO_3·2H_2O$). By contrast, pH 9 fluids lack thermonatrite and instead form trona and nahcolite ($NaHCO_3$). From pH 11 fluids, the mineralogy produced by slow-freezing is similar to that produced by flash-freezing, despite the latter crystallizing from a glass-like phase following re-warming. At pH 9 however, flash-frozen samples lack the nahcolite present in the slow-frozen samples.

## 4. Discussion

### 4.1. Partitioning of Ice and Nonice Components

Our results show that when fluids based on Enceladus' ocean composition are flash-frozen at rates exceeding 10 K s$^{-1}$, an ice-templated brine vein network is established, into which solutes are excluded. The exact cooling rate at a given point within a droplet is difficult to determine, but modeling of cooling within droplets of radii up to ~1 mm show that inferred cooling rates increase exponentially in the outer ~200 μm of a droplet (Ando et al., 2018; Song et al., 2010). This is consistent with smaller ice grain void sizes observed near the surface of flash-frozen droplets (Figure 1e), likely reflecting more rapid cooling than the bulk droplet. The release of intact solidified vein networks from ice by sublimation (Figures 1f and 1g) suggests that such ice-free cryogenic precipitates could exist in the vicinity of Enceladus or in Saturn's E ring, where plasma sputter erosion is known to preferentially erode water ice (Johnson et al., 2008).

**Table 3**
*Eutectic Mineral Assemblages Predicted by FREZCHEM, in g kg(H₂O)⁻¹*

| Formula | Mineral | pH 9 | | pH 11 | |
|---------|---------|------|------|-------|------|
| | | Fractional | Equilibrium | Fractional | Equilibrium |
| $H_2O$ | Ice | 989.991 | 991.687 | 980.178 | 980.193 |
| $NaCl_2 \cdot H_2O$ | Hydrohalite | 20.389 | 20.390 | 18.629 | 18.629 |
| $Na_2CO_3 \cdot 10\ H_2O$ | Sodium carbonate decahydrate | 2.672 | – | 20.029 | 20.029 |
| $NaHCO_3$ | Nahcolite | 4.950 | 6.520 | – | – |
| $KCl$ | Sylvite | 0.134 | 0.134 | 0.167 | 0.167 |
| $SiO_2$ | Amorphous silica | 0.199 | 0.166 | – | – |
| $NH_4Cl$ | Ammonium chloride | 0.054 | 0.054 | – | – |

### 4.2. Kinetic Inhibition of Crystallization During Flash Freezing

Our results show that if rapid cooling ($>10$ K s⁻¹) is sustained down to 77 K (approximate Enceladus surface temperature), ice and a glass-like noncrystalline phase are the two main products (Figures 1a–1e). The observation of evenly distributed bubbles (Figure 2a) within a smooth material resistant to sublimation suggests freeze-concentrated brine vitrifies at ice grain boundaries, forming an aqueous glass, where the bubbles represent gases that exsolve at, or before, vitrification of the liquid brine. Glass formation requires that fluids pass through a supercooled liquid phase, where crystal nucleation is kinetically impeded below the homogenous nucleation temperature (Wowk, 2010). This can be achieved by rapid cooling, through the addition of solutes which increase fluid viscosity, or by confinement of the fluid in micro-porous spaces where molecular rearrangement is restricted (Gallo et al., 2016). Combinations of these factors increase the chance for kinetic inhibition of crystallization.



**Figure 5.** X-ray diffraction patterns collected from crystalline cryogenic salts at both pH levels following contrasting freezing profiles. Identified peaks are: H, Halite (NaCl); S, Sylvite (KCl); Tr, Trona (Na₂CO₃·NaHCO₃·2H₂O); Th, Thermonatrite (Na₂CO₃·H₂O); N, Nahcolite (NaHCO₃). Note the largest halite peaks at 37.0 and 53.5° (2θ) are truncated for clarity.

Due to the high favorability of water ice crystallization, avoiding homogenous crystal nucleation in pure water requires cooling rates exceeding $10^6$ K s⁻¹ (Hallbrucker & Mayer, 1988). As this rate is faster than those achieved during our experiments, we assume that the portion of the experimental flash-frozen droplet not concentrated into brine veins (approximately 95 vol. %, based on brine volume dimensions) comprises crystalline water ice (ice $I_c$ and/or $I_h$), formed at or around the homogenous nucleation temperature of ice ($\sim$223 K). This is supported by previous work showing that crystallinity approaches 100% for pure water droplets of radius $\approx$ 1 mm flash frozen in LN₂ (Song et al., 2010). However, the production of noncrystalline material in our flash-frozen experiments show that conditions in the remaining droplet volume ($<$5 vol. %) can rapidly become prohibitive for further crystallization, as solutes are both highly concentrated and confined into ice grain boundaries. Similar partial vitrification behavior has been observed following brine vein supercooling in dilute Na-Cl solutions at cooling rates far below those required to vitrify the bulk solution (Imrichová et al., 2019).

Brine veins are concentrated around 20 times from their initial composition, based on inferred volume, but could retain the ion ratios of the original composition, thus being supersaturated with respect to several minerals. These freeze-concentrated fluids show a strong tendency for kinetic crystal inhibition, as they do not crystallize at 173 K even at slow cooling rates of 0.01 K s⁻¹ (Figure 2b), when frozen as a restricted thin film. Only when larger fluid volumes ($\geq$250 µl) are cooled slowly, do they behave in a manner approximated by FREZCHEM predictions. Differences between thin-film experiments and larger volume gradual cooling experiments are likely due to degree of connectivity in the brine vein network; thin
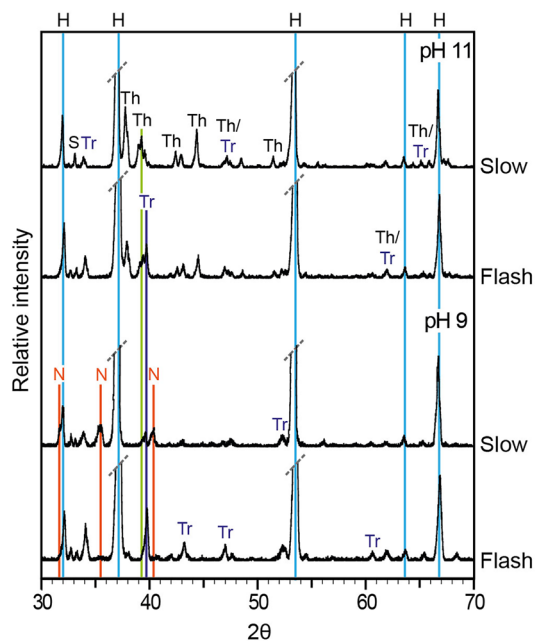
film cooling produces brine veins that are restricted in the vertical direction and thus are mostly entirely enclosed. Larger fluid volumes allow for the establishment of interconnected brine veins (Movie S1).

### 4.3. Production of Crystalline Materials Within Brine Veins

### 4.3.1. Direct Crystallization versus Crystallization Upon Warming

Based on our results, crystalline salts can form within the confines of brine veins through two contrasting routes: direct crystallization during cooling (produced by the slow freezing regime), or crystallization upon warming of previously supercooled or vitrified brine. Brine veins produced by the experimental slow freezing regime are larger, and thus less concentrated in solutes, than those in flash-frozen samples (Figures 1f and 1g). This supports the interpretation that crystalline salts had precipitated at or near saturation in the slow freezing regime, rather than further concentrating into a super-saturated brine.

Our results agree with previous studies of freezing in Na, Cl and $CO_3$-rich aqueous systems relevant to Ceres and an early Enceladus (Quick et al., 2019; Vu et al., 2017; Zolotov, 2007, 2017), showing that if cooled slowly, Enceladus′ ocean fluids should precipitate Na-carbonates and Na-chlorides. Detailed imaging of crystallization textures (Figures 2d and 2f) and compositions (Figure 3) in combination with FREZCHEM simulations (Figure 4) permit new insights not possible in these previous studies. We propose that after ice formation, which begins at ∼271 K in slow freezing experiments (Figure S1), the early precipitation of Na-carbonates produces a slurry of crystals in suspension within the brine veins, depleting the remaining brine in $CO_3^{2-}$/$HCO_3^-$. As the eutectic point is neared, Na and K (and minor $NH_4$) chloride minerals form, restricting space and forcing the Na-carbonate crystals into aggregates (Figures 2d and 2f). The resulting crystallization textures, expressed here at the 10 µm scale, are similar to eutectic solidification textures formed in igneous and metallic systems (Akamatsu & Plapp, 2016), thus we conclude they record the final solidification of the system at the eutectic. We also note that in pH 9 fluids, small filiform carbonates can morphologically resemble common terrestrial microorganisms (Figure 3d), with cautionary implications for interpreting potential microfossils in cryogenic particles (Fox-Powell et al., 2018).

The heterogenous mineral textures in slow-frozen samples contrast with the randomly distributed 10 µm scale textures observed in the flash-frozen samples following sublimation and re-warming (Figures 2f and 2g). These latter textures reflect the rapidity at which the system solidified, with crystal growth of different phases occurring simultaneously and/or in fixed positions, rather than in a sequence that allows for partitioning and aggregation of crystal suspensions. Crystal growth upon warming of a supercooled or vitrified fluid can progress directly from glass (similar to the formation of spherulites from glass in silicate igneous systems; Watkins et al., 2009) or from a metastable supercooled brine (Imrichová et al., 2019). Either process requires nucleation cores for crystal growth, hence we consider the rapid formation and incorporation of micro-crystals and/or silica nanoparticles into brine veins during flash-freezing as likely, where they can template later crystal growth when increased temperatures permit.

The observation of silica nanoparticles in the vicinity of Enceladus requires that the ocean is supersaturated with amorphous silica (Hsu et al., 2015). FREZCHEM predictions at pH 9 show that aqueous silica still in solution near the ocean surface should also precipitate as amorphous silica when freezing begins (Figure 4). Colloidal opal-A was not observed in our experimental samples at either cooling rate or pH, but the association of Si with the early forming Na-carbonates in experimental samples at pH 9 and 11 (Figures 3b and 3c) shows that it likely precipitates early. We suggest colloidal silica either nucleates, or co-precipitates, with the Na-carbonates, and thus is not directly observable by SEM. By the time chloride minerals form, Si is depleted in the remaining brine solution, explaining its reduced association with chloride minerals (Figure 3).

### 4.3.2. Mineralogy of Cryogenic Salts

Mineral assemblages produced by both experimental freezing regimes are consistent with those inferred from CDA measurements at Enceladus (i.e., Na-chlorides, Na-carbonates and minor K salts) (Postberg et al., 2009). While the CDA can probe only bulk composition, our experiments allow specific mineral phases to be compared and differentiated between contrasting cooling regimes and pH (Figure 5).

Experimental mineral assemblages produced by the slow freezing regime agree well with fractional and equilibrium FREZCHEM predictions from pH 11 fluids, where the carbonate mineralogy is dominated by $CO_3^{2-}$ phases. Dehydration during sublimation may account for differences in hydration state between predicted and observed minerals. Variation in carbonate mineralogy between pH 11 and pH 9 fluids likely reflects the pH-dependent speciation of DIC in solution. FREZCHEM runs indicate that in pH 11 fluids, as cooling progresses, $CO_3^{2-}$ dominates over $HCO_3^-$ until close to the eutectic, driving $Na_2CO_3$ mineral precipitation, while at pH 9, $HCO_3^-$ remains the dominant ion throughout cooling, allowing $NaHCO_3$ to accumulate (Figure S2). Together, our theoretical and experimental data therefore demonstrate that cryogenic carbonate assemblages in plume particles could be used as an independent pH probe for Enceladus' ocean for future missions, with the appearance of $Na_2CO_3$ phases indicative of parent fluid pH > 9.

At pH 9, fractional and equilibrium crystallization predictions differ. Despite initially beginning to precipitate in the equilibrium scenario, $Na_2CO_3 \cdot 10H_2O$ redissolves and does not appear in the final mineral assemblage (Table 3). A likely cause of this behavior is that the removal of $HCO_3^-$ ions upon nahcolite precipitation leads to protonation of aqueous $CO_3^{2-}$, leaving the brine undersaturated with respect to $Na_2CO_3 \cdot 10H_2O$. Based on these predictions, the appearance of $Na_2CO_3$ minerals in frozen pH 9 fluids would serve as evidence of fractional crystallization. The appearance of nahcolite and absence of $Na_2CO_3 \cdot 10H_2O$ or thermonatrite in experimental slow-frozen pH 9 fluids therefore suggests freezing progresses close to equilibrium crystallization conditions. However, we note the possible minor presence of trona ($Na_2CO_3 \cdot NaHCO_3 \cdot 2H_2O$) which was not predicted by either fractional or equilibrium crystallization scenarios. A previous study investigating the early freezing of Enceladus' ocean and establishment of the icy shell predicted trona formation *via* equilibrium crystallization (Zolotov, 2007), but these fluids bore an initial pH of ~10 and a lower concentration of $Na^+$ than used here, among other differences. The retention of this $Na_2CO_3$—bearing phase in the final mineral assemblage may therefore indicate some fractional crystallization behavior. This result is unsurprising considering the cooling rates employed here (~0.01 K $s^{-1}$); experimental efforts that achieve near equilibrium crystallization in terrestrial seawater have required much slower cooling rates (e.g., <1 K $h^{-1}$) (Butler & Kennedy, 2015), and/or long equilibration times (e.g., several weeks) (Marion et al., 1999).

In flash-frozen pH 9 samples, nahcolite is not observed in XRD patterns, despite being predicted as a major phase under both equilibrium and fractional crystallization conditions. Instead, trona is the major Na-carbonate, acting as a sink for both $CO_3^{2-}$ and $HCO_3^-$ ions. This suggests that $NaHCO_3$ formation has been inhibited by rapid cooling. Hence for lower pH Enceladus fluids, the presence of nahcolite is an indicator of more gradual freezing, while its absence might implicate supercooling and crystallization upon warming. From pH 11 fluids, the mineralogy produced by the slow freezing regime is similar to that produced by flash-freezing, suggesting that at higher pH, there is no compositional imprint of the supercooling/crystallization-upon-warming route to mineral formation. The evidence for such a process would therefore lie in crystal textures only.

Kinetic factors are also thought to influence mineral assemblages at Ceres; for example, flash-frozen experimental cryomagmas preferentially form ammonium salts not observed from slow freezing (Thomas et al., 2019). However, experimental Ceres-relevant fluids at pH ~9 preferentially form Na-carbonate phases over bicarbonates (Vu et al., 2017), contrary to our findings, and cryomagma evolution at Ceres is likely strongly influenced by ammonium, which is not currently identified as a component of Enceladus' plume particles (Postberg et al., 2009).

Finally, $KHCO_3$ has also been suggested as a product of freezing from an early ocean on Enceladus (Zolotov, 2007). In our fluids, which were designed based on modern plume particle compositions, the brine remains undersaturated with respect to $KHCO_3$ at all stages of freezing. Instead, sylvite (KCl) is the sole K-bearing mineral, appearing in all model runs and XRD patterns across all experimental samples. These results therefore indicate that, if crystalline salts exit within plume particles at Enceladus, all K is most likely present as sylvite.
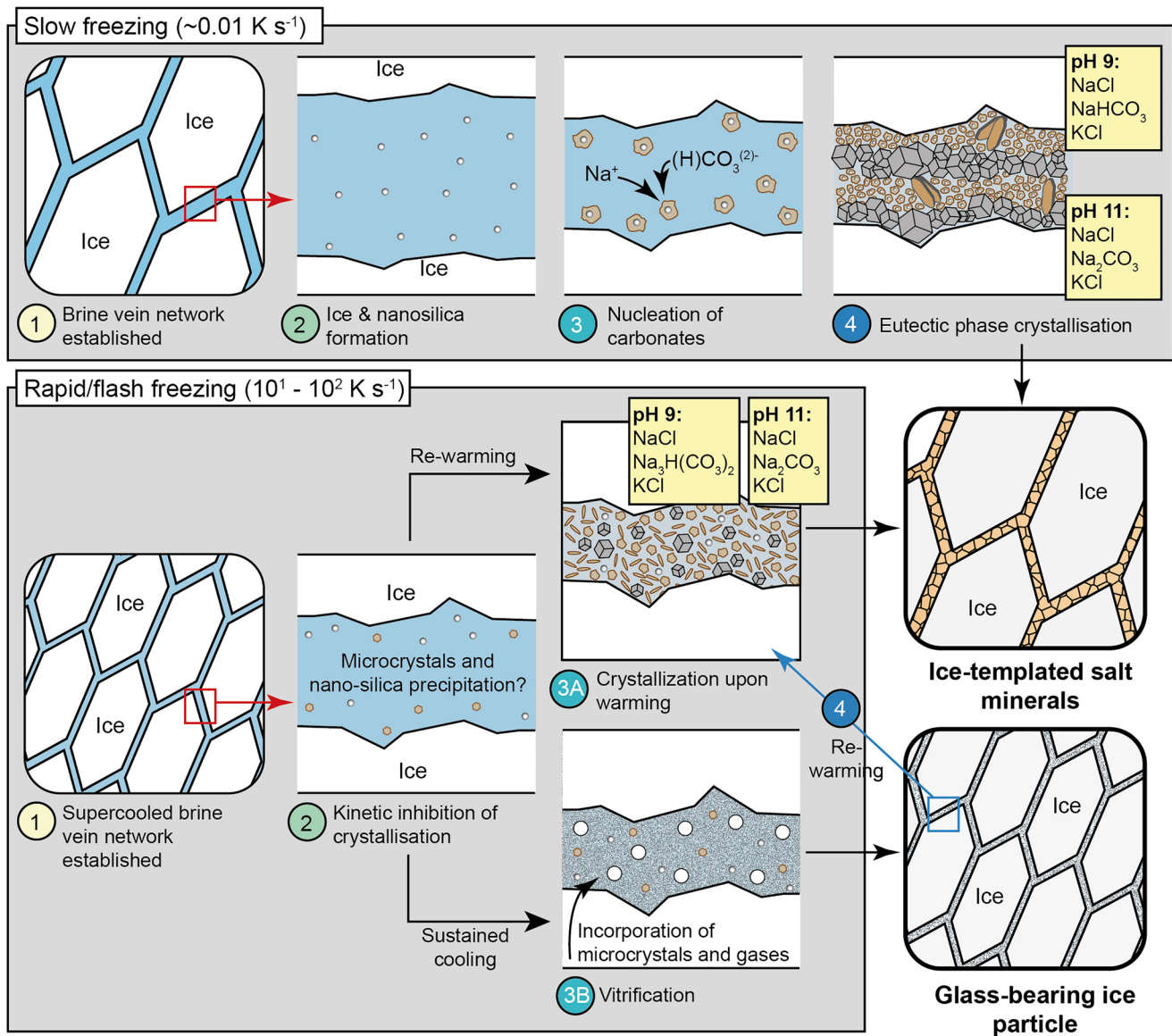
**Figure 6.** Possible routes for solid phase production during freezing of Enceladus' ocean fluids. Minerals identified by X-ray diffraction may be hydrates at cryogenic temperatures, thus ionic chemical formulae only are given here; potential hydration states are ignored.

### 4.4. Implications for the Plumes of Enceladus

Our experiments describe contrasting scenarios for solid phase production upon cooling of fluids with an Enceladean ocean composition (Figure 6), each of which leaves a compositional and textural signature of its formation route. Similar mechanisms may operate in the subsurface source region of the Enceladus plumes, or during the gradual incorporation of ocean fluids into the icy shell. Whether glass or crystalline material form in the plumes at Enceladus depends on the thermal history of ocean aerosols as they travel upwards from the liquid/vapor interface to space. Type III particles in the Enceladus plumes are thought to originate as evaporatively cooled 1–10 μm-sized aerosols (Porco et al., 2017; Postberg et al., 2009, 2011). Evaporative cooling of droplets in this size range can produce freezing rates of $10^4$ K s$^{-1}$ (Smith et al., 2006), significantly faster than those achieved during our flash-freezing experiment (13.9–63.3 K s$^{-1}$), suggesting that kinetic supercooling may be possible. However, because the vapor pressure of the droplets will decrease dramatically with temperature, and because these rates are not high enough to avoid homogenous ice nucleation (Hallbrucker & Mayer, 1988), evaporative cooling is effectively self-limiting, halting at or around

the homogenous ice nucleation temperature (~223 K). This differs from our flash-freezing experiments, in which rapid cooling continued down to ~77 K.

Rapid cooling however is not the only pathway to vitrification; confinement of fluid in microporous spaces can also inhibit crystallization (Gallo et al., 2016). Other studies have noted that with certain solute compositions and/or supersaturation during confinement, vitrification can occur without the need for excessively rapid cooling rates (Imrichová et al., 2019; Toner et al., 2014). Correspondingly, our results show that when fluid is confined into restrictive brine veins, crystallization is avoided, even at gradual cooling rates of 0.01 K s$^{-1}$, down to 172.98 K (Figure 2b), which is below the temperature of the surface of the tiger stripes (~197 K; Goguen et al., 2013). If particles cool to this point, they would be erupted into space and continue to lose heat. How brine vein partitioning scales to smaller droplet sizes is unknown, but partitioning in some form is still expected; for example, vein networks have been observed in flash-frozen droplets of CsCl brine at sizes closer to that of Enceladus' plume particles ($r \approx 80$ μm) (Vetráková et al., 2019). Thus, the conditions for crystal inhibition due to confinement may be met. Observations of the plumes by Cassini's Visible and Infrared Mapping Spectrometer (VIMS) show only evidence for crystalline ice (Dhingra et al., 2017), although as brine veins in flash-frozen samples can account for <5 vol. %, a minor amorphous component which may not be detectable by VIMS cannot be ruled out. Investigating the glass transition dynamics of the freeze-concentrated brine vein fluid will allow better assessments of the likelihood of cryovolcanic glass at Enceladus.

Our results show that if supercooled fluids are re-warmed, secondary crystalline salts can form. Given current constraints on vent thermal conditions, re-warming is likely; droplets evaporatively cooled to the homogenous ice nucleation temperature will be at a lower temperature than the ambient environment in the deeper parts of the vents (Nakajima & Ingersoll, 2016), thus may re-warm through conduction. Furthermore, if vapor condenses onto the particles, this can import heat. Icy particles encountered by Cassini that consist of pure water ice or ice and organics imply that condensation occurs throughout some portion of the crack depth (Postberg et al., 2011, 2018).

Due to the self-limiting nature of evaporative cooling and the likelihood of re-warming a conservative assumption is that crystalline salts are more likely than glass in the Enceladus plumes. Based on our experiments, these can precipitate in sequence, in a manner approximated by equilibrium crystallization predictions, or simultaneously in a kinetically limited manner, with implications for the mineralogy and distribution of salt phases (Figure 6). In the former scenario, mineral distribution is highly heterogenous at the scale of plume particles encountered by Cassini (sub-10 μm), with unknown consequences for inter- and intra-plume particle compositional variation. In the latter scenario, simultaneous crystallization leads to relatively homogenous mineral distribution. If the salt mineralogy of the plumes can be determined, either *via* remote sensing techniques or by in situ instrumentation on future missions, our results allow for the discrimination between these two routes to crystallization.

Finally, each route to producing solid phases from Enceladus' ocean fluids carries different implications for the capture of ocean constituents, including organic compounds. As the molecular organization of a glass resembles that of the liquid phase (Wowk, 2010), glasses represent a homogenous, unfractionated snapshot of fluid composition. Furthermore, the production of glass at Enceladus would provide an ideal mechanism for preserving macromolecular organic matter or microorganisms alongside their geochemical context. On the other hand, mineral formation, whether in sequence or simultaneous, may destroy biological structure and sequester organic matter within salt phases in a heterogenous manner.

## 5. Conclusions

This study provides constraints on endmember scenarios for solid phase production from Enceladus-relevant fluids. It is possible that a range of different plume particles with varied thermal histories, and therefore varied solid phase proportions, coexist, particularly at lower altitudes in the plumes where the particle size distribution may differ significantly from that recorded by the CDA (Porco et al., 2017). If crystalline material exists, its mineralogical composition and micron-scale partitioning can record fluid pH and delineate between thermodynamically defined crystallization in sequence, and kinetically limited simultaneous

crystallization. Based on these findings, nondestructive measurements of plume particles could open powerful new avenues of investigation at Enceladus and other bodies that display evidence for cryovolcanic processes, such as Ceres or Jupiter's moon Europa.

## Data Availability Statement

All data in support of these findings are available in Fox-Powell and Cousins (2020).

## References

Adda-Bedia, M., Kumar, S., Lechenault, F., Moulinet, S., Schillaci, M., & Vella, D. (2016). Inverse Leidenfrost effect: Levitating drops on liquid nitrogen. *Langmuir*, *32*(17), 4179–4188. https://doi.org/10.1021/acs.langmuir.6b00574

Akamatsu, S., & Plapp, M. (2016). Eutectic and peritectic solidification patterns. *Current Opinion in Solid State & Materials Science*, *20*(1), 46–54. https://doi.org/10.1016/J.COSSMS.2015.10.002

Ando, K., Arakawa, M., & Terasaki, A. (2018). Freezing of micrometer-sized liquid droplets of pure water evaporatively cooled in a vacuum. *Physical Chemistry Chemical Physics*, *20*(45), 28435–28444. https://doi.org/10.1039/c8cp05955a

Butler, B. M., & Kennedy, H. (2015). An investigation of mineral dynamics in frozen seawater brines by direct measurement with synchrotron X-ray powder diffraction. *Journal of Geophysical Research: Oceans*, *120*, 5686–5697. https://doi.org/10.1002/2015JC011032

Caldwell, D. R. (1974). Thermal conductivity of sea water. *Deep-Sea Research and Oceanographic Abstracts*, *21*(2), 131–137. https://doi.org/10.1016/0011-7471(74)90070-9

Channing, A., & Butler, I. B. (2007). Cryogenic Opal-A deposition from Yellowstone hot springs. *Earth and Planetary Science Letters*, *257*(1–2), 121–131. https://doi.org/10.1016/j.epsl.2007.02.026

Choblet, G., Tobie, G., Sotin, C., Běhounková, M., Čadek, O., Postberg, F., & Souček, O. (2017). Geophysical data from the Cassini spacecraft imply the presence of a global ocean underneath the ice shell of Enceladus 1, only a few kilometres below the surface in the south polar powering prolonged hydrothermal activity inside Enceladus. *Nature Astronomy*, *1*, 841–847. https://doi.org/10.1038/s41550-017-0289-8

Deamer, D., & Damer, B. (2017). Can life begin on Enceladus? A perspective from hydrothermal chemistry. *Astrobiology*, *17*(9), 834–839. https://doi.org/10.1089/ast.2016.1610

Dhingra, D., Hedman, M. M., Clark, R. N., & Nicholson, P. D. (2017). Spatially resolved near infrared observations of Enceladus' tiger stripe eruptions from Cassini VIMS. *Icarus*, *292*, 1–12. https://doi.org/10.1016/j.icarus.2017.03.002

Eugster, H. P., & Hardie, L. A. (1978). Saline Lakes. *Lakes*, *1*, 237–293. https://doi.org/10.1007/978-1-4757-1152-3_8

Fox-Powell, M. G., Channing, A., Applin, D., Cloutis, E., Preston, L. J., & Cousins, C. R. (2018). Cryogenic silicification of microorganisms in hydrothermal fluids. *Earth and Planetary Science Letters*, *498*, 1–8. https://doi.org/10.1016/j.epsl.2018.06.026

Fox-Powell, M. G., & Cousins, C. R. (2020). Data in support of manuscript titled: Partitioning of crystalline and amorphous phases during freezing of simulated Enceladus ocean fluids. *Mendeley Data*, *V1*. https://doi.org/10.17632/spmww2myjs.1

Gallo, P., Amann-Winkel, K., Angell, C. A., Anisimov, M. A., Frédé, F., Caupin, F., et al. (2016). Water: A Tale of two liquids. *Chemical Reviews*, *116*(46), 7463–7500. https://doi.org/10.1021/acs.chemrev.5b00750

Glein, C. R., Baross, J. A., & Waite, J. H. (2015). The pH of Enceladus' ocean. *Geochimica et Cosmochimica Acta*, *162*, 202–219. https://doi.org/10.1016/j.gca.2015.04.017

Glein, C. R., & Waite, J. H. (2020). The carbonate geochemistry of Enceladus' ocean. *Geophysical Research Letters*, *47*(3), e2019GL085885. https://doi.org/10.1029/2019gl085885

Goguen, J. D., Buratti, B. J., Brown, R. H., Clark, R. N., Nicholson, P. D., Hedman, M. M., et al. (2013). The temperature and width of an active fissure on Enceladus measured with Cassini VIMS during the 14 April 2012 South Pole flyover. *Icarus*, *226*(1), 1128–1137. https://doi.org/10.1016/j.icarus.2013.07.012

Hallbrucker, A., & Mayer, E. (1988). Vitrified dilute aqueous solutions. 2. Thermal behavior of hyperquenched sodium chloride-water and ethylene glycol-water glasses. *Journal of Physical Chemistry*, *92*(7), 2007–2012. https://doi.org/10.1021/j100318a059

Hendrix, A. R., Hurford, T. A., Barge, L. M., Bland, M. T., Bowman, J. S., Brinckerhoff, W., et al. (2019). The NASA Roadmap to ocean worlds. *Astrobiology*, *19*(1), 1–27. https://doi.org/10.1089/ast.2018.1955

Hsu, H.-W., Postberg, F., Sekine, Y., Shibuya, T., Kempf, S., Horányi, M., et al. (2015). Ongoing hydrothermal activities within Enceladus. *Nature*, *519*(7542), 207–210. https://doi.org/10.1038/nature14262

Imrichová, K., Veselý, L., Gasser, T. M., Loerting, T., Neděla, V., & Heger, D. (2019). Vitrification and increase of basicity in between ice Ih crystals in rapidly frozen dilute NaCl aqueous solutions. *Journal of Chemical Physics*, *151*(1). https://doi.org/10.1063/1.5100852

Johnson, R. E., Famá, M., Liu, M., Baragiola, R. A., Sittler, E. C., & Smith, H. T. (2008). Sputtering of ice grains and icy satellites in Saturn's inner magnetosphere. *Planetary and Space Science*, *56*(9), 1238–1243. https://doi.org/10.1016/J.PSS.2008.04.003

Johnson, P. V., Hodyss, R., Vu, T. H., & Choukroun, M. (2019). Insights into Europa's ocean composition derived from its surface expression. *Icarus*, *321*, 857–865. https://doi.org/10.1016/J.ICARUS.2018.12.009

King, P. L., Lescinsky, D. T., & Nesbitt, H. W. (2004). The composition and evolution of primordial solutions on Mars, with application to other planetary bodies. *Geochimica et Cosmochimica Acta*, *68*(23), 4993–5008. https://doi.org/10.1016/j.gca.2004.05.036

Marion, G., Farren, R., & Komrowski, A. (1999). Alternative pathways for seawater freezing. *Cold Regions Science and Technology*, *29*(3), 259–266. https://doi.org/10.1016/S0165-232X(99)00033-6

Marion, G., Mironenko, M. V., & Roberts, M. W. (2010). FREZCHEM: A geochemical model for cold aqueous solutions. *Computers & Geosciences*, *36*(1), 10–15. https://doi.org/10.1016/J.CAGEO.2009.06.004

McKay, C. P., Anbar, A. D., Porco, C., & Tsou, P. (2014). Follow the plume: The habitability of Enceladus. *Astrobiology*, *4*, 352–355. https://doi.org/10.1089/ast.2014.1158

Nakajima, M., & Ingersoll, A. P. (2016). Controlled boiling on Enceladus. 1. Model of the vapor-driven jets. *Icarus*, *272*, 309–318. https://doi.org/10.1016/j.icarus.2016.02.027

Porco, C. C., Dones, L., & Mitchell, C. (2017). Could it Be snowing microbes on Enceladus? Assessing conditions in its plume and implications for future missions. *Astrobiology*, *17*(9), 876–901. https://doi.org/10.1089/ast.2017.1665

Porco, C. C., Helfenstein, P., Thomas, P. C., Ingersoll, A. P., Wisdom, J., West, R., et al. (2006). Cassini observes the active south pole of Enceladus. *Science*, *311*(5766), 1393–1401. https://doi.org/10.1126/science.1123013

Postberg, F., Kempf, S., Schmidt, J, Brilliantov, N., Beinsen, A., Abel, B., et al. (2009). Sodium salts in E-ring ice grains from an ocean below the surface of Enceladus. *Nature*, *459*(June), 1–4. https://doi.org/10.1038/nature08046

Postberg, F., Khawaja, N., Abel, B., Choblet, G., Glein, C. R., Gudipati, M. S., et al. (2018). Macromolecular organic compounds from the depths of Enceladus. *Nature*, *558*(7711), 564–568. https://doi.org/10.1038/s41586-018-0246-4

Postberg, F., Schmidt, J., Hillier, J., Kempf, S., & Srama, R. (2011). A salt-water reservoir as the source of a compositionally stratified plume on Enceladus. *Nature*, *474*(7353), 620–622. https://doi.org/10.1038/nature10175

Quick, L. C., Buczkowski, D. L., Ruesch, O., Scully, J. E. C., Castillo-Rogez, J., Raymond, C. A., et al. (2019). A possible brine reservoir beneath occator crater: Thermal and compositional evolution and formation of the cerealia dome and vinalia faculae. *Icarus*, *320*, 119–135. https://doi.org/10.1016/j.icarus.2018.07.016

Reh, K., Spilker, L., Lunine, J. I., Waite, J. H., Cable, M. L., Postberg, F., & Clark, K. (2016). Enceladus life finder: The search for life in a habitable moon. *IEEE aerospace conference proceedings* (pp. 1–8). https://doi.org/10.1109/AERO.2016.7500813

Sharqawy, M. H., Lienhard, J. H., & Zubair, S. M. (2010). Thermophysical properties of seawater: A review of existing correlations and data. *Desalination and Water Treatment*, *16*, 354–380. Retrieved from http://web.mit.edu/lienhard/www/Thermophysical_properties_of_seawater-DWT-16-354-2010.pdf

Smith, J. D., Cappa, C. D., Drisdell, W. S., Cohen, R. C., & Saykally, R. J. (2006). Raman thermometry measurements of free evaporation from liquid water droplets. *Journal of the American Chemical Society*, *128*(39), 12892–12898. https://doi.org/10.1021/ja063579v

Song, Y. S., Adler, D., Xu, F., Kayaalp, E., Nureddin, A., Anchan, R. M., et al. (2010). Vitrification and levitation of a liquid droplet on liquid nitrogen. *Proceedings of the National Academy of Sciences*, 107(10), 4596–4600. https://doi.org/10.1073/pnas.0914059107

Taubner, R.-S., Pappenreiter, P., Zwicker, J., Smrzka, D., Pruckner, C., Kolar, P., et al. (2018). Biological methane production under putative Enceladus-like conditions. *Nature Communications*, *9*, (748), 1–11. https://doi.org/10.1038/s41467-018-02876-y

Thomas, E. C., Hodyss, R., Vu, T. H., Johnson, P. V., & Choukroun, M. (2017). Composition and evolution of frozen chloride brines under the surface conditions of Europa. *Earth and Space Chemistry*, *1*, 14–23. https://doi.org/10.1021/acsearthspacechem.6b00003

Thomas, P. C., Tajeddine, R., Tiscareno, M. S., Burns, J. A., Joseph, J., Loredo, T. J., et al. (2016). Enceladus's measured physical libration requires a global subsurface ocean. *Icarus*, *264*, 37–47. https://doi.org/10.1016/J.ICARUS.2015.08.037

Thomas, E. C., Vu, T. H., Hodyss, R., Johnson, P. V., & Choukroun, M. (2019). Kinetic effect on the freezing of ammonium-sodium-carbonate-chloride brines and implications for the origin of Ceres' bright spots. *Icarus*, *320*, 150–158. https://doi.org/10.1016/J.ICARUS.2017.12.038

Toner, J. D., Catling, D. C., & Light, B. (2014). The formation of supercooled brines, viscous liquids, and low-temperature perchlorate glasses in aqueous solutions relevant to Mars. *Icarus*, *233*, 36–47. https://doi.org/10.1016/j.icarus.2014.01.018

Toner, J. D., Catling, D. C., & Light, B. (2015). Modeling salt precipitation from brines on Mars: Evaporation versus freezing origin for soil salts. *Icarus*, *250*, 451–461. https://doi.org/10.1016/j.icarus.2014.12.013

Tosca, N. J., & McLennan, S. M. (2006). Chemical divides and evaporite assemblages on Mars. *Earth and Planetary Science Letters*, *241*(1–2), 21–31. https://doi.org/10.1016/j.epsl.2005.10.021

Vetráková, U., Neděla, V., Runštuk, J., & Heger, D. (2019). The morphology of ice and liquid brine in an environmental scanning electron microscope: A study of the freezing methods. *The Cryosphere*, *13*, 2385–2405. https://doi.org/10.5194/tc-13-2385-2019

Vu, T. H., Choukroun, M., Hodyss, R., & Johnson, P. V. (2020). Probing Europa's subsurface ocean composition from surface salt minerals using in-situ techniques. *Icarus*, 113746, *349*. https://doi.org/10.1016/j.icarus.2020.113746

Vu, T. H., Hodyss, R., Johnson, P. V., & Choukroun, M. (2017). Preferential formation of sodium salts from frozen sodium-ammonium-chloride-carbonate brines – implications for Ceres' bright spots. *Planetary and Space Science*, *141*, 73–77. https://doi.org/10.1016/j.pss.2017.04.014

Waite, J. H., Glein, C. R., Perryman, R. S., Teolis, B. D., Magee, B. A., Miller, G., et al. (2017). Cassini finds molecular hydrogen in the Enceladus plume: Evidence for hydrothermal processes. *Science*, *356*(6334), 155–159. https://doi.org/10.1126/science.aai8703

Waite, J. H., Lewis, W. S., Magee, B., Lunine, J. I., McKinnon, W. B., Glein, C. R., et al. (2009). Liquid water on Enceladus from observations of ammonia and 40Ar in the plume. *Nature*, *460*(7259), 1164. https://doi.org/10.1038/nature08352

Watkins, J., Manga, M., Huber, C., & Martin, M. (2009). Diffusion-controlled spherulite growth in obsidian inferred from $H_2O$ concentration profiles. *Contributions to Mineralogy and Petrology*, *157*(2), 163–172. https://doi.org/10.1007/s00410-008-0327-8

Wowk, B. (2010). Thermodynamic aspects of vitrification. *Cryobiology*, *60*(1), 11–22. https://doi.org/10.1016/J.CRYOBIOL.2009.05.007

Zolotov, M. Y. (2007). An oceanic composition on early and today's Enceladus. *Geophysical Research Letters*, *34*(23), 1–5. https://doi.org/10.1029/2007GL031234

Zolotov, M. Y. (2012). Aqueous fluid composition in CI chondritic materials: Chemical equilibrium assessments in closed systems. *Icarus*, *220*(2), 713–729. https://doi.org/10.1016/j.icarus.2012.05.036

Zolotov, M. Y. (2017). Aqueous origins of bright salt deposits on Ceres. *Icarus*, *296*, 289–304. https://doi.org/10.1016/j.icarus.2017.06.018

Zolotov, M. Y., & Shock, E. L. (2001). Composition and stability of salts on the surface of Europa and their oceanic origin. *Journal of Geophysical Research*, *106*(E12), 32815–32827. https://doi.org/10.1029/2000JE001413